Article

Not peer-reviewed version

Preliminary Mineralogical Characterization of Mercury Ore from the Karoli Orebody, Idrija Deposit (Slovenia): Implications for Ore Genesis

Gal Bubnič * , Jorge L. Costafreda , Domingo A. Martin

Posted Date: 27 February 2026

doi: 10.20944/preprints202602.1221.v1

Keywords: LA-ICP-MS; pyrite; Idrija mercury deposit; mercury; trace elements

 doi:10.20944/preprints202602.1221.v1

Article

Preliminary Mineralogical Characterization of Mercury Ore from the Karoli Orebody, Idrija Deposit (Slovenia): Implications for Ore Genesis

Gal Bubnič [1,*], Jorge L. Costafreda [2] and Domingo A. Martín [2]

[1] Department of Geology, Faculty of Natural Sciences and Engineering, University of Ljubljana, Aškerčeva 12, 1000 Ljubljana, Slovenia
[2] Escuela Técnica Superior de Ingenieros de Minas y Energía, Universidad Politécnica de Madrid, C/Ríos Rosas, 21, 28003 Madrid, Spain
* Correspondence: gb78843@student.uni-lj.si

Abstract

The Idrija mercury deposit represents one of the largest mercury formations globally, ranking second only to the Almadén deposit in Spain. The deposit has been exploited for more than five centuries and represents one of the most historically significant and extensively studied mercury mines worldwide. The Karoli orebody is characterized by a high abundance of pyrite (from 50 to 90%) and exceptionally rich cinnabar mineralization, with mercury contents locally reaching up to 78%. This study aims to provide a preliminary yet detailed characterization of the ores from the Idrija mercury deposit and to establish their textural and genetic characteristics. We implemented microscopic examination of thin sections, complemented by LA-ICP-MS trace element analyses of pyrite. Three different pyrite types were identified: fine-grained framboidal Py1, subhedral to euhedral Py2, and larger, well-developed euhedral Py3. LA-ICP-MS analysis of Py3 pyrite grains revealed low trace element concentrations, with maximum values remaining below 100 ppm. These observations suggest that the hydrothermal fluids were mercury-rich but of low salinity, which may have limited the incorporation of trace elements into pyrite. Our research provides new insights into the formation of the Karoli orebody. We envision that further investigations of fluid composition, salinity, and fluid inclusions could significantly enhance understanding of the Idrija mercury formation and evolution.

Keywords: LA-ICP-MS; pyrite; Idrija mercury deposit; mercury; trace elements

1. Introduction

The Idrija mine ranks among the world's largest mercury deposits, second only to the Almadén mine in Spain in terms of total mercury production. It is situated in the western part of Slovenia (Figure 1), within a geologic setting characterized by complex nappe structures and fault zones. The deposit is composed of sedimentary rocks that were deformed and fragmented into blocks during Middle Triassic rifting [1].

In contrast, the Almadén mercury deposit is hosted mainly by volcanic and volcano-sedimentary rocks (e.g. [2]), whereas the third-largest mercury district, Monte Amiata in Italy, is associated with magmatically influenced sedimentary rocks (e.g. [3]).

The Karoli tectonic unit (Figure 2) represents a distinct section of the Idrija ore deposit, characterized by a lenticular orebody. It contains high-grade mercury mineralization, with the Jeklenka ore reaching concentrations of up to 78%. Pyrite is abundant as well, comprising 50–90% of the rock [4,5].

Extensive research on the geology of the Idrija mercury deposit was carried out throughout the previous century [1,4–11]. With the advancement of analytical methods, researchers began applying geochemical techniques to the study of the Idrija deposit. Lavrič and Spangenberg [12] applied carbon, oxygen, and sulfur isotope analyses to various host rocks and minerals to determine the

 doi:10.20944/preprints202602.1221.v1

sources of fluids and the nature of hydrothermal alteration. Their study demonstrated that the Idrija hydrothermal system was fracture-controlled and involved interaction between deep-seated fluids and host dolomites. Their isotopic evidence suggests a mixed meteoric–seawater and magmatic fluid origin, with multiple sulfur sources responsible for the observed δ^{34}S heterogeneity. Another study by Božič et al. [13] investigated the range of mercury isotopic compositions from the Idrija mine to improve the understanding of Hg tracing within the ore deposit. They found that the mercury isotopic composition of the Idrija mine shows considerable variability, both between and within excavation sites, with δ^{202}Hg ranging from −1.35 to 0.46‰ and Δ^{199}Hg from −0.16 to 0.18‰. In addition, their results indicate that individual sites may be relatively homogeneous. However, the mine as a whole cannot be characterized by a single isotopic fingerprint, pointing to the complexity of Hg distribution.

Pyrite is a ubiquitous sulfide mineral that forms in a wide range of ore systems and remains stable under diverse physicochemical conditions. This provides valuable insights for reconstructing ore-forming processes and genetic evolution [14–16]. Pyrite can incorporate a wide spectrum of trace elements, including V, Cr, Mn, Co, Ni, Cu, Ga, As, Ag, Cd, Sb, Au, Tl, and Pb, which can be measured in situ using laser ablation inductively coupled plasma mass spectrometry (LA-ICP-MS) (e.g. [17–21]). The study by Gregory et al. [22], which analyzed more than 1,400 pyrites from more than 40 shales and sediments, provided important insights into the mechanisms of trace element incorporation in pyrite.

Sulfur isotope compositions provide key constraints on sulfide origins and fluid sources. Accordingly, δ^{34}S values can differentiate microbial sulfate reduction, thermochemical sulfate reduction, and magmatic–hydrothermal contributions [23,24]. Incorporating sulfur isotopes therefore enhances reconstruction of ore-forming processes in sediment-hosted hydrothermal systems.

Mercury isotopes experience both mass-dependent (MDF, usually presented as δ^{202}Hg) and mass-independent fractionation (usually presented as Δ^{199}Hg), which together provide valuable insights into the sources and cycling of Hg in surface environments [25–27]. More importantly, sedimentary, diagenetic, hydrothermal and metamorphic processes do not contribute to Hg mass-independent fractionation (MIF), allowing Δ^{199}Hg values in sedimentary records to be used for reconstructing Hg geochemical cycles through geological time [28,29].

This study was motivated by the work of Božič et al. [13], who noted that the Karoli orebody lies in one of the deepest parts of the Idrija mine and that its ore genesis has not been sufficiently investigated. The laser ablation–inductively coupled plasma–mass spectrometry (LA-ICP-MS) was applied to pyrite from the Karoli ore zone to gain further insights into the ore genesis and the processes responsible for the formation of the Karoli orebody. Results from LA-ICP-MS analysis suggest that Pb exhibits the highest median concentration (21.92 ppm), followed by Ni (17.92 ppm) and As (10.78 ppm).

2. Geological Setting

Idrija mercury mine is located in W Slovenia, about 35 km W from Ljubljana. In general, Slovenia has a very complex geological setting, characterized by many faults and thrusts, especially in the western part. Western Slovenia is dominated by 2 mountain ranges: the Northern part consists of Southern Alps, while the Southern part is bordered by the External Dinarides. The area of Idrija deposit consists of highly deformed sedimentary rocks (Figure 1), which originally formed part of the Slovenian carbonate platform. This platform subsequently fragmented into blocks by deep faults due to E-W trending Middle Triassic rifting [1,30]. The rifting led to the consolidation of the Julian and Dinaric carbonate platforms to the north and south, respectively, and the development of a more deeply subsided Slovenian Basin in the central part [31].

The Idrija ore deposit developed within the Idrija tectonic system, which originated during the Middle Triassic. Mineralization developed in an anticline structure, likely associated with a laccolith intrusion of unknown composition [10]. The tectonic system was oriented in an east-west direction. The structure consisted of northern and southern sedimentary zones separated by corresponding sill, with the Idrija Middle Triassic tectonic trench situated between them. Ore-bearing rocks were formed

 doi:10.20944/preprints202602.1221.v1

on the northern and southern sills as well as within the tectonic trench [11]. The Triassic sequence developed unconformably above Permo-Carboniferous organic-rich black shales and Upper Permian sandstones, shales and dolomites. The sequence consists of Lower Scythian dolomites, Upper Scythian shales, limestones and dolomites, Anisian dolomite and Langobardian shales, sandstones, limestones and pyroclastites [1].

The current tectonic configuration of Slovenia's territory emerged during the Tertiary orogenic period, resulting from the collision between the Apulian lithospheric plate and the Eurasian lithospheric plate [32]. This collision led to the overthrusting of the Apulian plate onto the Eurasian plate, which resulted in a prevailing N–S oriented recent principal stress direction within the territory of Slovenia. This led to the formation of a network of complementary strike-slip faults, the most notable and known being the Idrija fault, which is still active today [33].

Tertiary thrusting occurred along a NNE–SSW direction, oblique to the principal axis of the Idrija tectonic system [34]. Thrust tectonics segmented the originally continuous ore-bearing zone into three distinct structural blocks. Furthermore, neotectonic faulting has subdivided the deposit into several blocks, with the largest and richest portion of the orebody displaced along the Idrija Fault. In addition, the faulting separated the deposit into the Idrija and Ljubevč segments, while simultaneously uplifting other sections of the deposit, which have been eroded [10].

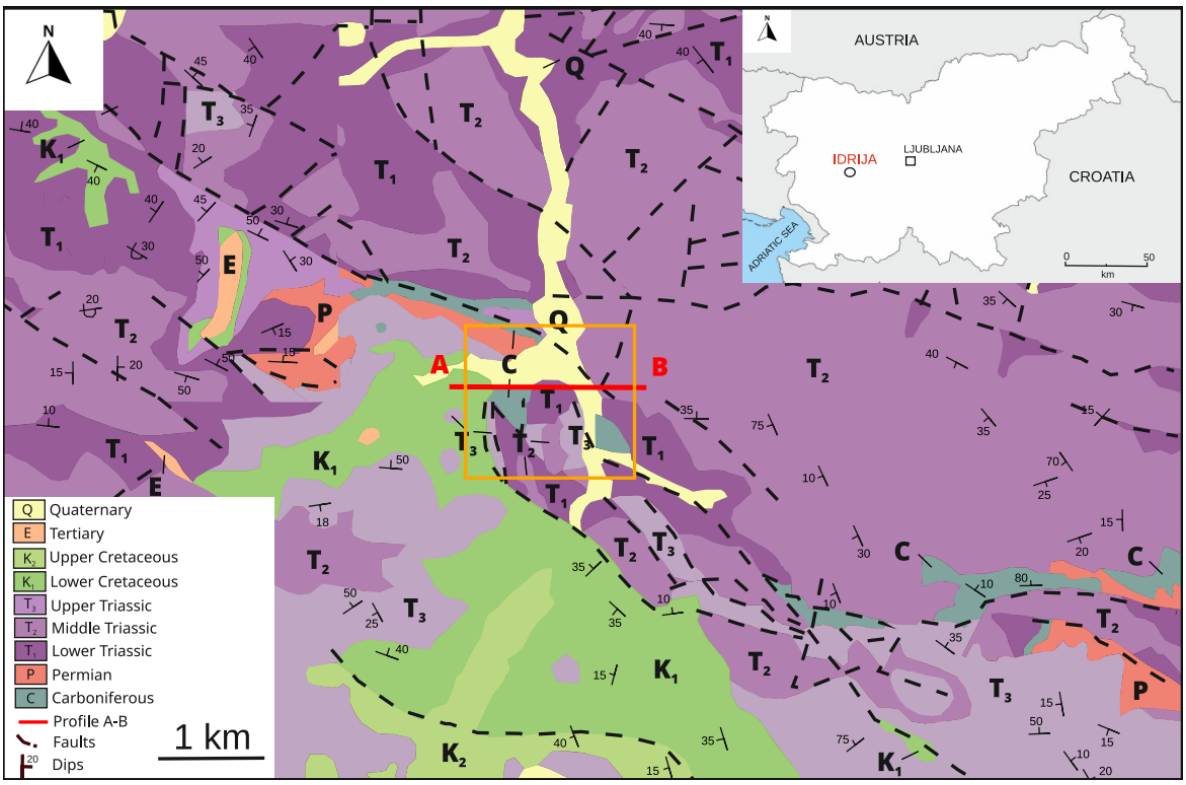

Figure 1. Regional geological map of the basic structural subdivision of the western Slovenia. The orange rectangle marks the study area around the Idrija ore deposit. The red line represents the approximate profile of the deposit, presented in Figure 2.

3. Ore Deposit Geology

Previous studies have established that the Idrija mercury deposit formed during the Middle Triassic, specifically in the Langobardian substage (e.g. [8,35]). The formation of mercury ore in Idrija deposit occurred in two stages [4]. During the first stage, rocks of Upper Paleozoic, Scythian, and Anisian age were subjected to mercury enrichment. The second phase involved the deposition of the Upper Ladinian *Skonca* beds and volcanic tuffs. During this stage, hydrothermal fluids further mineralized the Permo-Carboniferous to Anisian strata and also affected the Upper Ladinian conglomerates. Mlakar and Drovenik [4] conducted a detailed study of the mineralogy and genesis of the deposit, the

 doi:10.20944/preprints202602.1221.v1

key findings of which are briefly summarized below. Carboniferous shale and sandstone are locally mineralized, particularly along their contact with Triassic strata, where they contain low-grade ore composed of cinnabar and native mercury. The Upper Permian dolomite represents one of the largest orebodies in the deposit, with individual bodies extending over several thousand square meters. Ore is generally low-grade, except along fault zones and fractures, where the highest-grade mineralization, such as the Jeklenka ore, is locally present. The Lower Scythian sequence is composed of dolomite, shale, siltstone, and oolitic limestone. The dolomite units are among the thickest in the deposit, locally reaching up to 170 m [5]. Oolitic limestone represents one of the most ore-enriched horizons, particularly where it occurs close to mineralized fractures or at intersections between these fractures and shale layers. The Upper Scythian dolomite is moderately mineralized, with orebodies typically developed along its contact with the overlying Upper Scythian limestone or immediately beneath the tectonic–erosional unconformity. In contrast, the Upper Scythian limestone is only weakly mineralized, containing minor amounts of cinnabar. Orebodies within the Anisian dolomite are associated with the tectonic–erosional unconformity, with the highest-grade cinnabar mineralization occurring directly beneath the Langobardian sandstone. The Langobardian sequence consists of a basal sandstone directly overlying the unconformity, followed by conglomerate, limestone, *Skonca* bed and tuff. The basal sandstone hosts small orebodies, yet the mineralization is of exceptionally high grade. The overlying conglomerate is very uniformly mineralized and contains high-grade ore with cinnabar and native mercury. In contrast, the limestone unit is largely barren, with only occasional cinnabar occurrences. One of the most ore-enriched horizons within the Langobardian succession is the *Skonca* shale and sandstone layer, where orebodies extend over 10 to 100 m and contain the highest-grade cinnabar mineralization and native mercury. The tuff and chert units also contain minor orebodies, though the ore is usually of a higher grade. The Cordevolian rocks represent the youngest lithological units within the deposit that are enriched, although the degree of mineralization is relatively low.

The Karoli orebody represents a distinct segment of the Idrija mercury deposit. It exhibits a lenticular shape ranging in areal extent from a few square meters up to 100 m^2, exceptionally rich cinnabar mineralization with mercury concentrations reaching up to 78% [4]. Pyrite is abundant, ranging from 50 to 90%, occurring mostly as reniform and spheroidal diagenetic concretions, as well as in smaller euhedral grains, measuring from 0,5 to 10 mm in size [5]. Cinnabar forms irregular grains and veinlets and locally replaces pyrite. The host rock is primarily sandstone that grades upward into bituminous shale and mudstone [36]. The highest-grade ore within the Karoli orebody occurs in *Skonca* layer, reaching the thickness of up to 40 m [37].

 doi:10.20944/preprints202602.1221.v1

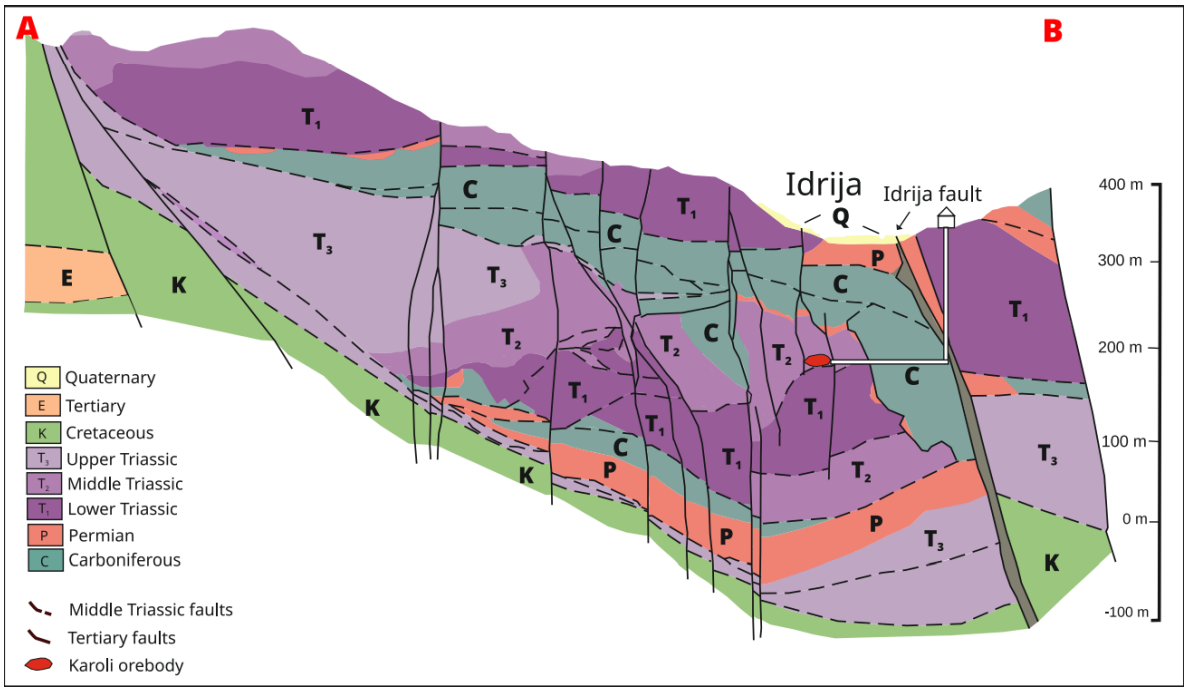

Figure 2. Schematic cross section along the profile A-B of the Idrija ore deposit (modified after [1,11,38]). The red lenticular shape represents the Karoli orebody. The shaft entrance and inclined shaft connecting the surface to the orebody are shown schematically, with a mining structure illustrated at the surface. Vertical scale is indicated; horizontal distances are approximate.

4. Materials and Methods

This section describes the materials and methods used to analyze the Karoli orebody, including sample preparation and analytical techniques.

4.1. Materials

Thin sections were prepared from rock samples collected from the Karoli orebody of the Idrija mercury deposit (western Slovenia). The rock contains multiple generations of pyrite and associated cinnabar. For this study, analyses focused on an euhedral Py3 pyrite grain due to its well-developed crystal morphology. The thin sections allowed microscopic observation and subsequent LA-ICP-MS analysis of trace-element concentrations.

4.2. Methods

Five polished thin-section samples (S-K-a, S-K-b, S-K-c, S-K-d and S-K-e) were prepared from an original volumetric sample for mineralogical study using reflected-light microscopy (Figure 3 a-e). Photomicrographs were acquired using a Nikon Eclipse E200 microscope equipped with a Nikon digital camera.

A modal mineralogical determination based on visual estimation under reflected-light microscopy was carried out to assess the mineralogical composition of the studied samples. Volumetric proportions of the ore minerals were estimated following the method proposed by Castroviejo [39] and are presented in Table 1.

Trace-element concentrations in pyrite were determined using laser ablation inductively coupled plasma mass spectrometry (LA-ICP-MS). Analyses were conducted on an euhedral Py3 pyrite grain from the Karoli orebody. A total of 18 spot analyses were performed on the same grain in order to assess trace-element contents and intra-grain variability.

All LA-ICP-MS measurements were carried out in the same laboratory using the same instrumentation and analytical protocol as described in Šoster et al. [40]. Detailed information on instrumental

 doi:10.20944/preprints202602.1221.v1

configuration, laser parameters, calibration standards, and data reduction procedures is provided in the aforementioned study and is not repeated here.

5. Results

To characterize the mineralogical and textural features of the Idrija ore and to constrain trace element distributions in pyrite, the samples were examined using reflected-light microscopy and analyzed by LA-ICP-MS. Reflected-light microscopy allowed detailed observation of pyrite textures and their relationships with cinnabar and gangue minerals, while LA-ICP-MS provided precise quantitative measurements of trace elements in pyrite. Together, these complementary methods provide a reliable basis for understanding the formation and evolution of the studied Karoli orebody.

5.1. Texture of Pyrite

Three main pyrite types can be observed in our sample (Figure 3 a-e). Py1 occurs as fine-grained framboidal disseminated aggregates, commonly surrounded by cinnabar that fills interstitial spaces between pyrite grains. Py2 consists of subhedral to locally euhedral pyrite crystals, typically showing more euhedral development along grain margins. The crystal surfaces are commonly coated by fine-grained particles interpreted as relic framboidal pyrite. Py3 occurs as coarse euhedral crystals reaching up to 10 mm in size. The grains commonly display veinlets and microfractures that cut across the crystal structure, suggesting formation in a post-sedimentary environment. Due to the elevated concentrations of cinnabar and mercury in the Py1 and Py2, trace element analyses using LA-ICP-MS were successfully conducted only on Py3.

Additionally, Py1, Py2, and Py3 show brecciated textures in which the mineral breaks down into small idiomorphic and xenomorphic fragments (Figure 3 a, b, d). Dissolution textures formed by the reaction of pyrite with cinnabar are common (Figure 3 a, d). Segregation textures are observed on the surface of the main pyrite phenocrystals (Figure 3 c, d). Granular-porphyritic and poikilitic textures also predominate, where the pyrite phenocrystals show marked idiomorphism (Figure 3 a, b, d). Finally, a visible banded and fluid texture is shown in Figure 3 a, b, d, and e.

The studied ores also contain cinnabar as the principal mercury-bearing mineral, accompanied by gangue minerals forming the host matrix. The dark gray to nearly black gangue assemblage includes sedimentary matrix, accessory minerals, and other unidentified components, as no transmitted-light microscopy or mineralogical analyses were conducted to specifically determine the gangue mineral assemblage.

Table 1 summarizes the modal mineral proportions of representative samples, estimated using the visual percentage method of Castroviejo [39]. Pyrite contents range from 10 to 60%, whereas cinnabar accounts for 5 to 30% of the samples. Gangue minerals and matrix phases together comprise approximately 15 to 65%.

 doi:10.20944/preprints202602.1221.v1

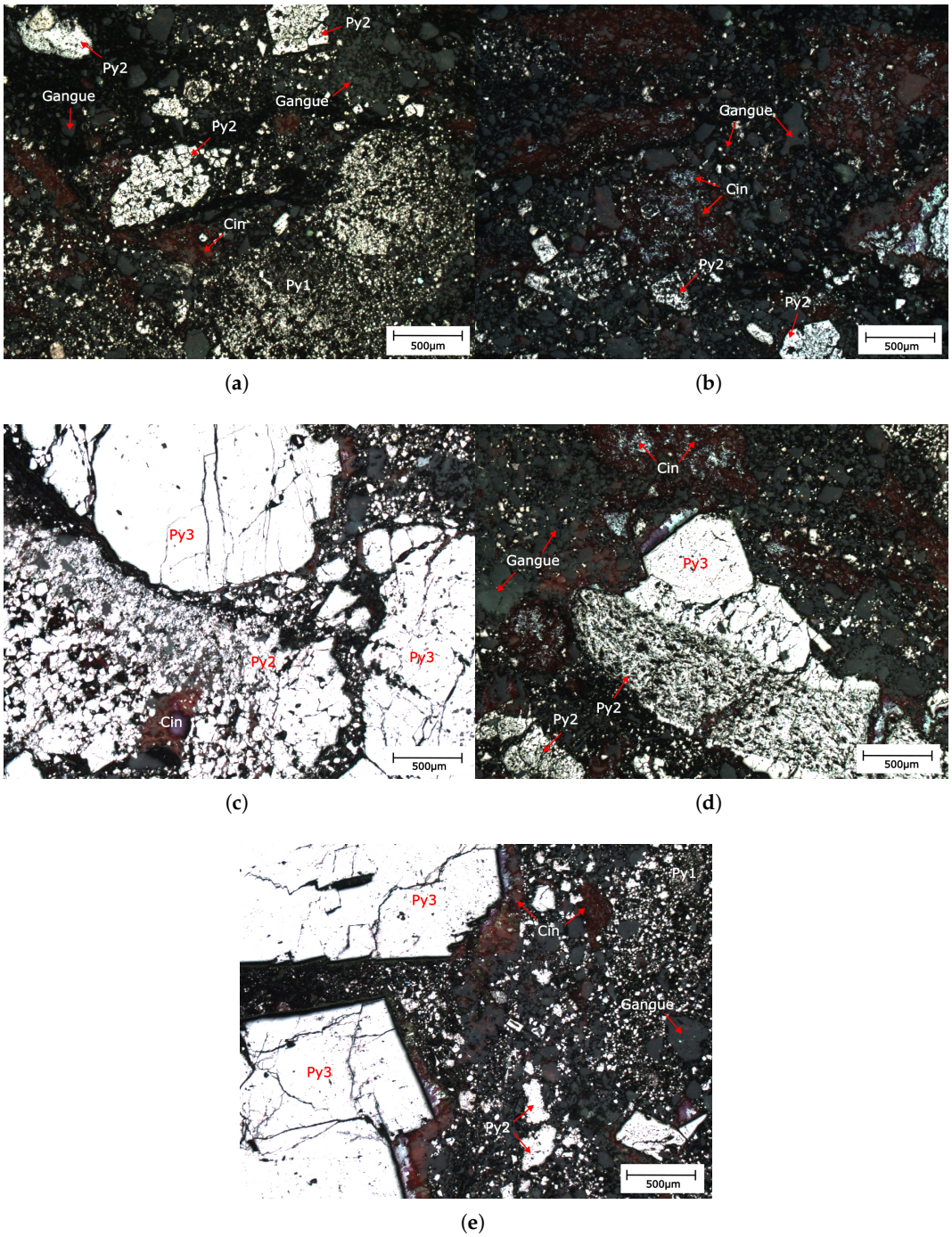

Figure 3. Reflected-light photomicrographs of Karoli ore pyrite: (**a**) Fine-grained pyrite (Py1) and coarser-grained, subhedral to locally euhedral pyrite (Py2). (**b**) Abundant cinnabar (Cin) associated with locally developed Py2. (**c**) Larger Py3 grain with smaller Py2 grains containing cinnabar in fractures. (**d**) Fine-grained Py2 in contact with larger, euhedral, cracked Py3 grains, with cinnabar present in fractures and veinlets within Py2. (**e**) Large, euhedral Py3 grains with fine-grained, framboidal Py1 and smaller subhedral to euhedral Py2 grains.

 doi:10.20944/preprints202602.1221.v1

Table 1. Estimated mineral percentages (pyrite, cinnabar, gangue) for representative photomicrographs of Karoli samples (Figure 3 a–e).

SAMPLE	PYRITE (%)	CINNABAR (%)	GANGUE (%)
S-K-a	30	5	65
S-K-b	10	30	60
S-K-c	60	25	15
S-K-d	35	20	45
S-K-e	55	5	40

5.2. LA-ICP-MS Results

A set of 18 spot analyses using LA-ICP-MS were carried out on pyrite samples Py3 from the Karoli orebody. Trace elements including V, Cr, Mn, Co, Ni, Cu, Ga, As, Ag, Cd, Sb, Au, Tl and Pb were measured above instrumented limits and are presented in Table 2. Correlation coefficients between trace elements in pyrite are summarized in Table 3. In addition, LA-ICP-MS trace element correlation plots for Ag-Pb, As-Ni, Co-Ni and Sb-Pb are presented in Figure 4.

Table 2. LA-ICP-MS results for Py3 from Karoli ore in Idrija deposit.

No.	V	Cr	Mn	Co	Ni	Cu	Ga	As	Ag	Cd	Sb	Au	Tl	Pb
PY1	0.24	0.74	0.27	0.94	17.95	4.26	-	9.17	0.019	-	2.02	0.025	0.62	27.57
PY2	0.11	0.39	0.24	1.76	36.18	4.22	-	12.93	0.035	-	2.73	-	0.55	39.38
PY3	0.12	0.60	0.22	2.21	46.66	4.74	-	15.30	-	-	6.18	-	0.30	65.15
PY4	0.26	-	0.54	1.41	29.31	8.35	0.067	14.26	-	-	2.00	-	0.82	33.79
PY5	0.13	-	0.24	0.87	17.88	8.91	-	9.16	0.048	-	2.81	-	1.01	39.18
PY6	0.42	0.70	0.24	0.78	15.28	5.22	0.060	8.03	-	-	1.59	-	0.56	23.46
PY7	0.099	-	0.26	1.75	33.63	4.48	-	14.09	0.027	-	0.89	-	0.24	21.81
PY8	0.14	-	0.38	2.22	44.54	8.35	-	18.93	-	-	2.13	-	1.68	49.83
PY9	0.14	-	0.23	0.53	10.63	3.63	-	9.89	0.014	-	0.68	-	0.64	12.87
PY10	0.13	-	0.22	0.63	12.86	1.67	-	9.82	0.016	-	1.36	-	0.32	16.74
PY11	0.11	0.60	0.18	0.85	17.14	1.62	-	9.73	-	-	0.78	-	0.05	11.60
PY12	0.12	-	0.25	0.61	13.64	1.58	-	10.37	-	-	2.79	-	0.45	28.63
PY13	0.16	-	0.38	0.72	14.64	2.08	-	11.19	0.028	-	1.66	-	0.30	20.92
PY14	0.23	0.58	0.33	0.40	7.41	4.32	-	6.48	0.014	0.35	1.19	-	2.21	11.20
PY15	0.15	0.54	0.23	-	4.30	-	0.027	4.71	0.020	-	1.01	-	2.20	8.18
PY16	0.085	-	0.18	3.72	46.98	4.53	-	13.68	0.032	-	1.59	-	0.27	20.25
PY17	0.051	-	0.18	3.52	52.72	-	-	21.73	0.023	-	0.85	-	0.25	13.78
PY18	0.040	0.38	0.18	4.38	76.69	-	-	23.41	0.026	-	1.12	-	0.16	22.02

Note: All values in ppm; "-" means below detection limit.

The trace element composition of Py3 shows generally low values, with the highest values belonging to Pb (8.18–65.15 ppm), Ni (4.30–76.69) and As (4.71–23.41). Moderately enriched elements include Cu (1.58–8.91), Sb (0.68–6.18), Co (0.40–4.38) and Tl (0.05–2.21), with low content of Cr (0.38–0.74), Mn (0.18–0.54), V (0.04–0.42) and Ag (0.014–0.048). Scattered detections of Ga, Cd, Au and Bi were recorded, though most concentrations remained below the detection limit. Elements such as Zn, Ge, Se, Mo, In, Sn and Te remained consistently below the detection limit in all measured spots.

 doi:10.20944/preprints202602.1221.v1

Table 3. Correlation coefficients between trace elements in Py3 from Karoli ore.

ELEMENT	V	Cr	Mn	Co	Ni	Cu	As	Ag	Sb	Tl
Cr	0.72									
Mn	0.44	0.34								
Co	−0.54	−0.69	−0.31							
Ni	−0.50	−0.61	−0.20	0.96						
Cu	0.23	0.13	0.48	0.31	0.40					
As	−0.51	−0.59	−0.05	0.88	0.93	0.40				
Ag	−0.36	−0,71	−0.12	0.23	0.29	0.70	0.18			
Sb	−0.01	0.06	0.06	0.01	0.18	0.21	0.08	0.73		
Tl	0.28	0.05	0.36	−0.30	−0.39	0.51	−0.40	−0.24	−0.09	
Pb	−0.01	−0.03	0.24	0.13	0.36	0.53	0.32	0.80	0.88	−0.07

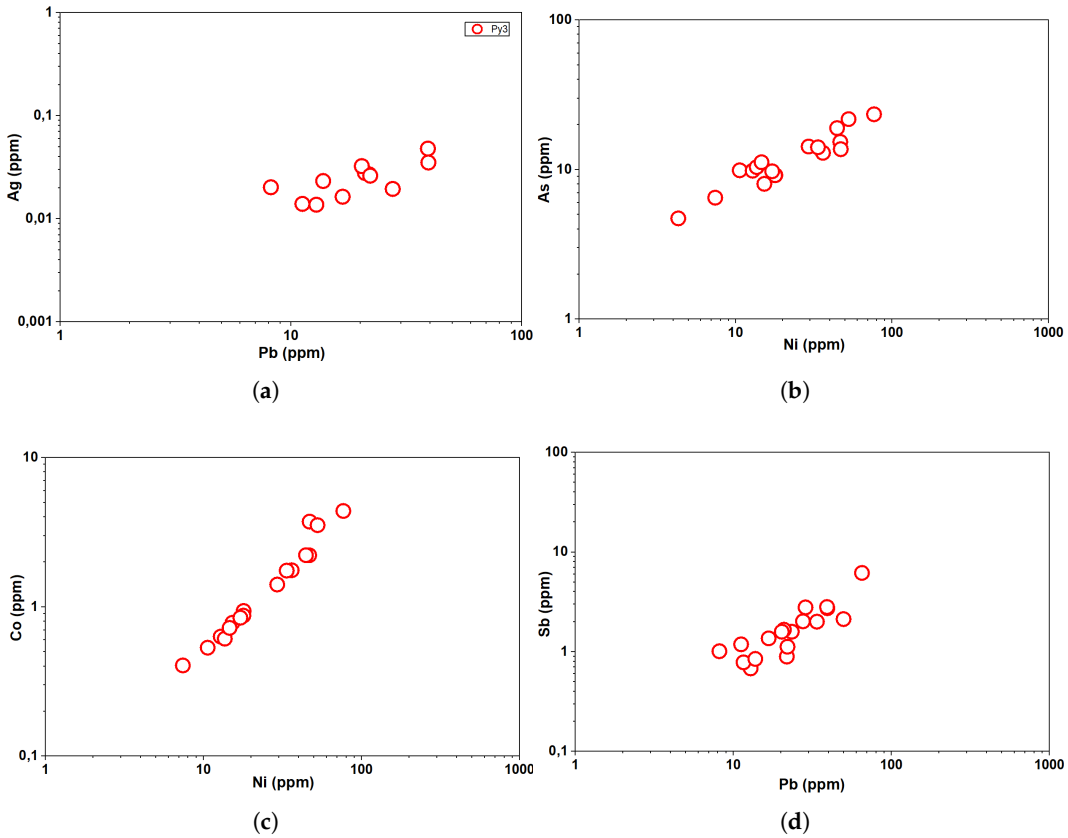

Figure 4. Py3 LA-ICP-MS trace element correlation plots for: (**a**) Ag-Pb. (**b**) As-Ni. (**c**) Co-Ni. (**d**) Sb-Pb.

6. Discussion

The following discussion interprets the geochemical and isotopic data obtained for the Karoli orebody, focusing on trace element composition, sulfur and mercury isotopes, and their implications for ore genesis.

6.1. Trace Element Composition

Lead is the most abundant element in our Karoli ore dataset (median value 21.92 ppm). It is rarely incorporated into the pyrite structure due to its large ionic size. As a result, galena may occur as inclusions formed prior to the crystallization of pyrite[41,42].

Nickel is second most abundant element with a median value of 17.92 ppm. It is commonly incorporated into pyrite, most likely through substitution for Fe at octahedral lattice sites [43]. In both sedimentary and orogenic pyrite, Ni is strongly incorporated into the crystal lattice, allowing for its retention during diagenetic recrystallization and subsequent pyrite growth [44,45]. High correlation

 doi:10.20944/preprints202602.1221.v1

with Co (r=0.96, Figure 4c) suggests that Co and Ni were incorporated into the pyrite structure through isomorphous substitution for Fe within the crystal lattice [46]. Furthermore, the Co/Ni ratio has regularly been used to distinguish the pyrite origin. According to Bajwah et al. [47], hydrothermal pyrite typically contains more than 400 ppm Co and displays a Co/Ni ratio > 1, while sedimentary pyrite is characterized by Co concentrations below 100 ppm and Co/Ni < 1. The Co/Ni ratio in Karoli pyrite is between 0,1 and 0,01 which points to the sedimentary origin of pyrite.

Arsenic is the third most abundant element with a median value of 10.78 ppm. Previous studies have confirmed the substitution of As for S [48,49]. In addition, Qian et al. [50] argue that As can also substitute Fe in a high-sulfidation epithermal deposits.

Values of Cu in Karoli ore pyrite are below 10 ppm, with a median of 4.32 ppm. Copper values in pyrite can be found ranging from a few ppm to wt % [51]. Reich et al. [43] noted that the incorporation of copper into the pyrite structure as a solid solution is limited, with maximum concentrations ranging between 1000 and 2000 ppm. Higher values are usually the result of micro to nano-inclusions of chalcopyrite. Low contents in Py3 could indicate low temperature fluids and precipitation of chalcopyrite which incorporated Cu (e.g. [52]).

Generally, antimony in pyrite was found as a structural impurity alongside Tl and Hg [53,54]. A strong positive correlation between Sb, Ag, and Pb in our sample (Figure 3) suggests that Sb is structurally incorporated into pyrite, potentially through a coupled substitution involving Ag [55]. Lower content of Sb in Karoli pyrite (median 1.59 ppm) could be the result of fluid cooling (around 150 °C), which lead to precipitation of stibnite [56].

Cobalt (median 0.94 ppm) is present in low concentrations having a strong correlation with Ni (0.96) and As (r=0.88). Maslennikov et al. [57] showed elevated sulfur fugacity and/or reduced temperatures favor the substitution of divalent cations for Fe^{2+} in pyrite, with Co^{2+} being preferentially incorporated compared to Ni^{2+}. Their study also found the pyrite with higher Ni values was present in low-temperature zone. The previously noted strong correlation with As may reflect the presence of both elements by a common hydrothermal fluid [58]. Elevated Co and Ni concentrations (>1000 ppm) in pyrite have been associated with the presence of micro-inclusions [59].

Thallium is present above the detection limit in all spots with a median of 0.50 ppm. The occurrence of Tl serves as a reliable indicator of low-temperature pyrite formation [57].

Manganese and vanadium are both present in concentrations below 1 ppm. Median for Mn is 0.24 and 0.13 for V, respectively. Because Mn and V are both highly soluble in fluids at moderate to high temperatures, their precipitation is favored under cooler conditions, making them valuable indicators of low-temperature mineralization [60]. The weak to moderate positive correlation between Mn and V suggests that both elements were introduced under similar conditions and likely co-precipitated during low-temperature fluid evolution.

Finally, Figure 5 compares median pyrite trace element concentrations for Idrija with those reported for Almadén [61]. Red circles (Almadén) are generally above gray squares (Idrija), reflecting differences in sulfide chemistry between the two deposits. Nevertheless, a similar trend can be recognized in the diagram. The concentrations of siderophile elements, such as Co and Ni, are comparatively close, particularly in the case of Ni (Figure 5). However, a noticeable difference is observed in the behavior of chalcophile elements (Cu, Cd, Sb, and As), and this contrast becomes even more pronounced for lithophile elements (V and Mn).

 doi:10.20944/preprints202602.1221.v1

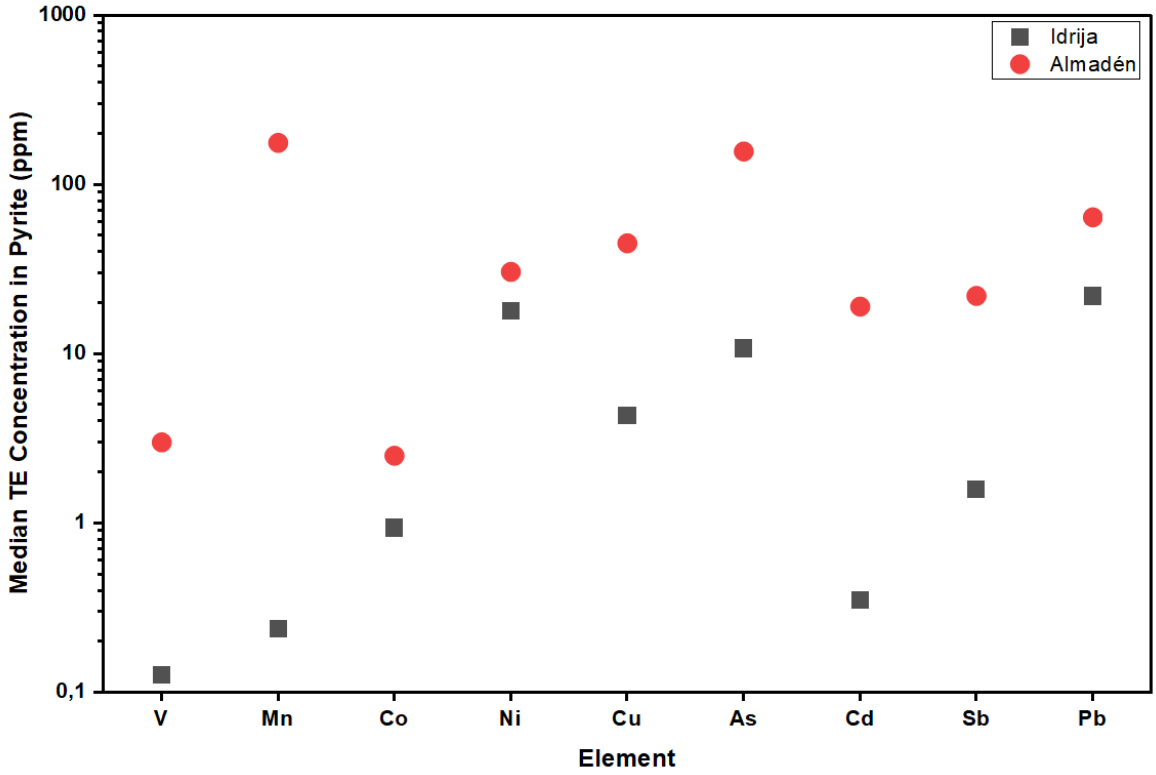

Figure 5. Median trace element concentrations (ppm) in pyrite from the Idrija deposit from our study (n = 18) and the Almadén deposit ([61], n = 6). Gray squares represent Idrija, red circles represent Almadén. Only elements with concentrations above detection limits in both deposits are shown.

6.2. Sulfur and Mercury Isotopes

Sulfur isotope data from Lavrič and Spangenberg [12] include 14 cinnabar and 24 pyrite samples from the Karoli orebody. Cinnabar $\delta^{34}S$ values range from +0.1 to +3.2‰ (median +0.8‰), while pyrite values range from −2.0 to +6.5‰ (median −1.2‰). Overall, the sulfide $\delta^{34}S$ values cluster near 0‰, consistent with a magmatic sulfur contribution (e.g. [23,24]), potentially related to regional Triassic volcanic activity.

Mercury isotope data for the Karoli ore, reported in Božič et al. [13], show $\Delta^{199}Hg = -0.06$ and $\delta^{202}Hg = -0.10$. Previous studies have shown that hydrothermal systems in continental-arc settings commonly display positive $\Delta^{199}Hg$ values, indicative of input from recycled Hg in subducted oceanic crust [26]. Therefore, the negative $\Delta^{199}Hg$ values are interpreted as reflecting upper-crustal recycling of continental Hg into an intracontinental hydrothermal system [62]. This is consistent with the passive-margin sedimentation of Slovenia throughout the Mesozoic.

6.3. Implications for Ore Genesis

Idrija ore deposit has been extensively investigated in the past. However, the genesis of Karoli orebody has not been definitively established. Although previous studies classify Idrija as a sedimentary-exhalative (SEDEX) deposit (e.g. [4]), our results allow for a more refined interpretation of the processes that shaped the Karoli orebody.

Three generations of pyrite are observed in the Karoli ore. The morphologies range from fine-grained framboidal Py1, subhedral to euhedral Py2 and larger euhedral Py3 grains. The presence of this morphologies have been most commonly observed in sedimentary pyrite [63]. The surfaces of Py2 crystals are commonly coated by fine-grained particles interpreted as relic framboidal pyrite (Py1). This indicates that Py2 grew as a partial overgrowth and recrystallization of earlier framboidal aggregates during late diagenetic evolution. Euhedral pyrite grains in our samples commonly exceed 1 mm, some even 10 mm, and display extensive networks of microcracks that are locally infilled with

 doi:10.20944/preprints202602.1221.v1

cinnabar. The cross-cutting relationship, in which fractures cut pyrite crystal faces and later host mercury mineralization, indicates that fracturing preceded cinnabar deposition and that the cracks served as conduits for Hg-bearing hydrothermal fluids.

The V/Cr ratio is commonly used as a proxy for redox conditions in sedimentary environments [64]. According to established thresholds, mentioned by Jones and Fike [65], values below 2 reflect oxic conditions, 2–4.25 indicate suboxic conditions, and ratios above 4.25 correspond to secondary oxic or anoxic environments. The V/Cr ratio measured in Karoli euhedral pyrite (Py3) is 0.21, indicating that the pyrite crystallized under relatively oxidizing conditions. As previously discussed, the Co/Ni ratios ranging from 0.01 to 0.1 in Py3 fall within the typical sedimentary pyrite range, indicating a sediment-derived origin for this generation of pyrite.

The measured euhedral Py3 exhibits very low trace-element concentrations, with Pb being the most enriched element (median around 22 ppm). This depletion is attributed to the oxidizing conditions during pyrite formation and the inferred low-salinity nature of the hydrothermal fluids, as evidenced by the absence of Se, Te, Ge, Mo, and Zn [66]. Under such conditions, both sulfide and chloride complexes necessary for transporting chalcophile elements were sparse, strongly limiting their incorporation into pyrite, causing low trace-element count in Karoli ore pyrite.

7. Conclusions

The Idrija ore deposit is one of the world's largest mercury accumulations, characterized by exceptionally high-grade cinnabar mineralization. In this study, LA-ICP-MS analyses of pyrite were used to investigate the genesis of the Karoli orebody.

The present research provides a preliminary mineralogical characterization of the Idrija mercury deposit, with a focus on trace element distributions in pyrite obtained via LA-ICP-MS. The results offer valuable insight into the formation and mineralization processes of one of the deposit's orebodies and may serve as a reference for future studies of Idrija and other mercury-bearing ore deposits, particularly those with a low trace element values. Overall, these findings contribute a strong framework for understanding ore formation and can guide both geochemical research and comparative studies in similar hydrothermal systems.

Our analysis suggests that low Co/Ni ratios (0.01–0.1) point to a sedimentary origin of the precursor pyrite, whereas V/Cr ratios confirm that the recrystallization environment was oxidizing. The extremely low trace-element contents, along with the systematic absence of Se, Te, Ge, and Mo, indicate low-salinity, Cl-poor fluids incapable of transporting or incorporating significant chalcophile elements into pyrite.

Finally, we envision future research focusing on fluid composition, salinity, and metal transport through targeted fluid-inclusion analyses and direct halogen measurements in coexisting gangue minerals, complemented by additional pyrite trace-element datasets to better constrain elemental behavior under variable fluid conditions.

Author Contributions: Conceptualization, G.B., J.L.C. and D.A.M.; methodology, G.B., J.L.C. and D.A.M.; software, G.B., J.L.C. and D.A.M.; validation, G.B., J.L.C. and D.A.M.; formal analysis, G.B., J.L.C. and D.A.M.; investigation, G.B., J.L.C. and D.A.M.; resources, G.B., J.L.C. and D.A.M.; data curation, G.B., J.L.C. and D.A.M.; writing—original draft preparation, G.B., J.L.C. and D.A.M.; writing—review and editing, G.B., J.L.C. and D.A.M.; visualization, G.B., J.L.C. and D.A.M.; supervision, G.B., J.L.C. and D.A.M.; project administration, G.B., J.L.C. and D.A.M.; funding acquisition, G.B., J.L.C. and D.A.M. All authors have read and agreed to the published version of the manuscript.

Funding: This research received no external funding.

Data Availability Statement: Data are contained within the article.

Acknowledgments: The authors gratefully acknowledge Aleš Šoster (University of Ljubljana) for providing the dataset used in this study and for his valuable assistance and contributions throughout the course of the research.

 doi:10.20944/preprints202602.1221.v1

Tim Sotelšek (University of Ljubljana) is acknowledged for assistance with the acquisition and interpretation of microscopic images.

Conflicts of Interest: The authors declare no conflicts of interest.

References

1. Čar, J.; Placer, L. The Middle Triassic structure of the Idrija region. *Geologija* **1977**, *20*, 141–166.
2. Higueras, P.; Oyarzun, R.; Lillo, J.; Morata, D. Intraplate mafic magmatism, degasification, and deposition of mercury: The giant Almadén mercury deposit (Spain) revisited. *Ore Geology Reviews* **2013**, *51*, 93–102.
3. Rimondi, V.; Chiarantini, L.; Lattanzi, P.; Benvenuti, M.; Beutel, M.; Colica, A.; Costagliola, P.; Di Benedetto, F.; Gabbani, G.; Gray, J.E.; et al. Metallogeny, exploitation and environmental impact of the Mt. Amiata mercury ore district (Southern Tuscany, Italy). *Italian Journal of Geosciences* **2015**, *134*, 323–336.
4. Mlakar, I.; Drovenik, M. Strukturne in genetske posebnosti idrijskega rudišča. *Geologija* **1971**, *14*, 67–126.
5. Drovenik, M.; Pleničar, M.; Drovenik, F. The origin of Slovenian ore deposits. *Geologija* **1980**, *23*, 1–157.
6. Čadež, F. Gypsum and anhydrite occurrences in Idria region. *Geologija* **1977**, *20*, 289–301.
7. Čadež, F. Najmlajše diskordantne sedimentne kamenine na karbonskih plasteh v Idriji. *Geologija* **1980**, *23*, 163–172.
8. Mlakar, I. Relations between the lower and the upper structure of the Idrija ore deposit. *Geologija* **1967**, *10*, 87–126.
9. Placer, L.; Čar, J. Rekonstrukcija srednjetriadnih razmer na idrijskem prostoru. *Geologija* **1975**, *18*, 197–209.
10. Placer, L. Structural history of the Idrija mercury deposit. *Geologija* **1982**, *25*, 7–94.
11. Čar, J. Angular tectonic-erosional unconformity in the deposit's part of the Idrija Middle Triassic tectonic structure. *Geologija* **1988**, *31*, 267–284.
12. Lavrič, J.V.; Spangenberg, J.E. Stable isotope (C, O, S) systematics of the mercury mineralization at Idrija, Slovenia: constraints on fluid source and alteration processes. *Mineralium Deposita* **2003**, *38*, 886–899.
13. Božič, D.; Živković, I.; Dizdarević, T.; Peljhan, M.; Štrok, M.; Horvat, M. Insights into the heterogeneity of the mercury isotopic fingerprint of the Idrija Mine (Slovenia). *Minerals* **2023**, *13*, 1227.
14. Agangi, A.; Hofmann, A.; Wohlgemuth-Ueberwasser, C.C. Pyrite zoning as a record of mineralization in the Ventersdorp Contact Reef, Witwatersrand Basin, South Africa. *Economic Geology* **2013**, *108*, 1243–1272.
15. Zhang, J.; Deng, J.; Chen, H.y.; Yang, L.q.; Cooke, D.; Danyushevsky, L.; Gong, Q.j. LA-ICP-MS trace element analysis of pyrite from the Chang'an gold deposit, Sanjiang region, China: Implication for ore-forming process. *Gondwana Research* **2014**, *26*, 557–575.
16. Thomas, H.V.; Large, R.R.; Bull, S.W.; Maslennikov, V.; Berry, R.F.; Fraser, R.; Froud, S.; Moye, R. Pyrite and pyrrhotite textures and composition in sediments, laminated quartz veins, and reefs at Bendigo gold mine, Australia: Insights for ore genesis. *Economic Geology* **2011**, *106*, 1–31.
17. Large, R.R.; Danyushevsky, L.; Hollit, C.; Maslennikov, V.; Meffre, S.; Gilbert, S.; Bull, S.; Scott, R.; Emsbo, P.; Thomas, H.; et al. Gold and trace element zonation in pyrite using a laser imaging technique: Implications for the timing of gold in orogenic and Carlin-style sediment-hosted deposits. *Economic Geology* **2009**, *104*, 635–668.
18. Large, R.R.; Halpin, J.A.; Danyushevsky, L.V.; Maslennikov, V.V.; Bull, S.W.; Long, J.A.; Gregory, D.D.; Lounejeva, E.; Lyons, T.W.; Sack, P.J.; et al. Trace element content of sedimentary pyrite as a new proxy for deep-time ocean–atmosphere evolution. *Earth and Planetary Science Letters* **2014**, *389*, 209–220.
19. Li, W.; Cook, N.J.; Xie, G.Q.; Mao, J.W.; Ciobanu, C.L.; Li, J.W.; Zhang, Z.Y. Textures and trace element signatures of pyrite and arsenopyrite from the Gutaishan Au–Sb deposit, South China. *Mineralium Deposita* **2019**, *54*, 591–610.
20. Deditius, A.P.; Utsunomiya, S.; Reich, M.; Kesler, S.E.; Ewing, R.C.; Hough, R.; Walshe, J. Trace metal nanoparticles in pyrite. *Ore Geology Reviews* **2011**, *42*, 32–46.
21. Gao, F.; Du, Y.; Pang, Z.; Du, Y.; Xin, F.; Xie, J. LA-ICP-MS trace-element analysis of pyrite from the Huanxiangwa gold deposit, Xiong'ershan district, China: Implications for ore genesis. *Minerals* **2019**, *9*, 157.
22. Gregory, D.D.; Large, R.R.; Halpin, J.A.; Baturina, E.L.; Lyons, T.W.; Wu, S.; Danyushevsky, L.; Sack, P.J.; Chappaz, A.; Maslennikov, V.V.; et al. Trace element content of sedimentary pyrite in black shales. *Economic Geology* **2015**, *110*, 1389–1410.
23. Seal, R.R. Sulfur isotope geochemistry of sulfide minerals. *Reviews in mineralogy and geochemistry* **2006**, *61*, 633–677.
24. Hoefs, J. *Stable isotope geochemistry*; Springer: Berlin, Germany, 2009.

 doi:10.20944/preprints202602.1221.v1

25. Bergquist, B.A.; Blum, J.D. Mass-dependent and-independent fractionation of Hg isotopes by photoreduction in aquatic systems. *Science* **2007**, *318*, 417–420.
26. Blum, J.D.; Sherman, L.S.; Johnson, M.W. Mercury isotopes in earth and environmental sciences. *Annual Review of Earth and Planetary Sciences* **2014**, *42*, 249–269.
27. Foucher, D.; Ogrinc.; Hintelmann, H. Tracing mercury contamination from the Idrija mining region (Slovenia) to the Gulf of Trieste using Hg isotope ratio measurements. *Environmental Science & Technology* **2009**, *43*, 33–39.
28. Grasby, S.E.; Them II, T.R.; Chen, Z.; Yin, R.; Ardakani, O.H. Mercury as a proxy for volcanic emissions in the geologic record. *Earth-Science Reviews* **2019**, *196*, 102880.
29. Moynier, F.; Jackson, M.G.; Zhang, K.; Cai, H.; Halldórsson, S.A.; Pik, R.; Day, J.M.; Chen, J. The mercury isotopic composition of Earth's mantle and the use of mass independently fractionated Hg to test for recycled crust. *Geophysical Research Letters* **2021**, *48*, e2021GL094301.
30. Buser, S. Stratigrafske vrzeli v paleozojskih in mezozojskih plasteh v Sloveniji. In Proceedings of the Regional geology and palaeontology symposium, 1980, pp. 335–345.
31. Buser, S. Development of the Dinaric and the Julian carbonate platforms and of the intermediate Slovenian Basin (NW Yugoslavia). *Mem. Soc. Geol. Ital* **1989**, *40*, 313–320.
32. Placer, L. Principles of the tectonic subdivision of Slovenia. *Geologija* **2008**, *51*, 205–217.
33. Gosar, A. Monitoring of micro-deformations along Idrija and Raša faults in W Slovenia. *Geologija* **2007**, *50*, 45–54.
34. Placer, L. Rekonstrukcija krovne zgradbe idrijsko žirovskega ozemlja. *Geologija* **1973**, *16*, 317–334.
35. Berce, B. Geologija živosrebrnega rudišča Idrija. *Geologija* **1958**, *4*, 5–62.
36. Čar, J. Ladinian skonca beds of the Idrija Ore Deposit (W Slovenia). *Geologija* **2013**, *56*, 151–174.
37. Čar, J. Razvoj srednjetriasnih sedimentov v idrijskem tektonskem jarku. Ph.d. thesis, University of Ljubljana, Univerza Edvarda Kardelja v Ljubljani, Fakulteta za naravoslovje in tehnologijo, Oddelek za geologijo, 1985.
38. Rečnik, A.; Čar, J.; Mirtič, B. *Minerals of the mercury ore deposit Idria*; Springer: Berlin, Germany, 2013.
39. Castroviejo, R. *Fundamentos de petrografía: Rocas ígneas, sedimentarias y metamórficas*; Red ALEMYMA-Programa ALFA (UE/DGI), Escuela Técnica Superior de Ingenieros de Minas, Universidad Politécnica de Madrid: Madrid, Spain, 1998. Unpublished teaching material from the Dpto. Ingeniería Geológica, 84 pp.
40. Šoster, A.; Erlandsson, V.B.; Ajuaba, S.; Šmuc, N.R. Selective trace element uptake in iron sulfides during burial metamorphism of coal: Insights from the coal-bearing Socka Beds, Northeastern Slovenia. *International journal of coal geology* **2025**, p. 104805.
41. Morse, J.; Luther Iii, G. Chemical influences on trace metal-sulfide interactions in anoxic sediments. *Geochimica et Cosmochimica Acta* **1999**, *63*, 3373–3378.
42. Koglin, N.; Frimmel, H.E.; Lawrie Minter, W.; Brätz, H. Trace-element characteristics of different pyrite types in Mesoarchaean to Palaeoproterozoic placer deposits. *Mineralium Deposita* **2010**, *45*, 259–280.
43. Reich, M.; Deditius, A.; Chryssoulis, S.; Li, J.W.; Ma, C.Q.; Parada, M.A.; Barra, F.; Mittermayr, F. Pyrite as a record of hydrothermal fluid evolution in a porphyry copper system: A SIMS/EMPA trace element study. *Geochimica et Cosmochimica Acta* **2013**, *104*, 42–62.
44. Large, R.R.; Maslennikov, V.V. Invisible gold paragenesis and geochemistry in pyrite from orogenic and sediment-hosted gold deposits. *Minerals* **2020**, *10*, 339.
45. Large, R.R.; Maslennikov, V.V.; Robert, F.; Danyushevsky, L.V.; Chang, Z. Multistage sedimentary and metamorphic origin of pyrite and gold in the giant Sukhoi Log deposit, Lena gold province, Russia. *Economic Geology* **2007**, *102*, 1233–1267.
46. Ai Zamruddin, N.N.S.; Zainal Abidin, N.S.; Endut, Z.; Makoundi, C.; Lok, L.K.; Ismail, M.S. Trace Element Analysis of Pyrite and Arsenopyrite Using the LA-ICPMS Technique in Pulai, Central Belt of Peninsular Malaysia. *Minerals* **2023**, *13*, 1026.
47. Bajwah, Z.; Seccombe, P.; Offler, R. Trace element distribution, Co: Ni ratios and genesis of the Big Cadia iron-copper deposit, New South Wales, Australia. *Mineralium Deposita* **1987**, *22*, 292–300.
48. Reich, M.; Kesler, S.E.; Utsunomiya, S.; Palenik, C.S.; Chryssoulis, S.L.; Ewing, R.C. Solubility of gold in arsenian pyrite. *Geochimica et Cosmochimica Acta* **2005**, *69*, 2781–2796.
49. Fleet, M.E.; Mumin, A.H. Gold-bearing arsenian pyrite and marcasite and arsenopyrite from Carlin Trend gold deposits and laboratory synthesis. *American Mineralogist* **1997**, *82*, 182–193.
50. Qian, G.; Brugger, J.; Testemale, D.; Skinner, W.; Pring, A. Formation of As (II)-pyrite during experimental replacement of magnetite under hydrothermal conditions. *Geochimica et Cosmochimica Acta* **2013**, *100*, 1–10.
51. Herazo, A.; Reich, M.; Barra, F.; Morata, D.; Real, I.d. Trace element geochemistry of pyrite from bitumen-bearing stratabound Cu–(Ag) deposits, Northern Chile. *ACS Earth and Space Chemistry* **2021**, *5*, 566–579.

 doi:10.20944/preprints202602.1221.v1

52. Keith, M.; Häckel, F.; Haase, K.M.; Schwarz-Schampera, U.; Klemd, R. Trace element systematics of pyrite from submarine hydrothermal vents. *Ore Geology Reviews* **2016**, *72*, 728–745.
53. Nyström, E.; Thomas, H.; Wanhainen, C.; Alakangas, L. Occurrence and release of trace elements in pyrite-rich waste rock. *Minerals* **2021**, *11*, 495.
54. Wang, Y.Y.; Long, T.; Fougerouse, D.; Liu, X.M.; Li, Q.; Yu, X.F.; Ma, M.Z.; Liu, D.Y. Heterogeneous incorporation of trace elements at the microscale and nanoscale during episodic epitaxial growth of pyrite. *Geological Society of America Bulletin* **2025**, *137*, 899–910.
55. Yu, Q.; Wang, Z.; Sun, Q.; Wang, K. In Situ Trace Element and Sulfur Isotope Composition of Pyrite from the Beiwagou Pb-Zn Deposit, Liaodong Peninsula, Northeast China: Implications for Ore Genesis. *Minerals* **2023**, *13*, 1176.
56. Zhang, Z.; Xie, G.; Olin, P. Texture, in-situ geochemical, and S isotopic analyses of pyrite and arsenopyrite from the Longshan Sb-Au deposit, southern China: Implications for the genesis of intrusion-related Sb-Au deposit. *Ore Geology Reviews* **2022**, *143*, 104781.
57. Maslennikov, V.; Maslennikova, S.; Large, R.; Danyushevsky, L. Study of trace element zonation in vent chimneys from the Silurian Yaman-Kasy volcanic-hosted massive sulfide deposit (Southern Urals, Russia) using laser ablation-inductively coupled plasma mass spectrometry (LA-ICPMS). *Economic Geology* **2009**, *104*, 1111–1141.
58. Abraitis, P.; Pattrick, R.; Vaughan, D. Variations in the compositional, textural and electrical properties of natural pyrite: a review. *International Journal of Mineral Processing* **2004**, *74*, 41–59.
59. Qin, Z.W.; Wang, L.; Qin, K.Z.; Li, G.M.; Xue, S.C.; Song, G.X. Geochemistry of trace elements of pyrite and its implications in intermediate sulfidation epithermal systems: Case study based on the Zhengguang Au–Zn deposit, North-East China. *Journal of Geochemical Exploration* **2025**, p. 107810.
60. Revan, M.K.; Genc, Y.; Maslennikov, V.V.; Maslennikova, S.P.; Large, R.R.; Danyushevsky, L.V. Mineralogy and trace-element geochemistry of sulfide minerals in hydrothermal chimneys from the Upper-Cretaceous VMS deposits of the eastern Pontide orogenic belt (NE Turkey). *Ore Geology Reviews* **2014**, *63*, 129–149.
61. Martín, J.A.; Lespagnard, J.M.; Maroto, A.G.; Galiano, J.G. Distribución geoquímica de elementos traza en los sulfuros pirita y cinabrio y en las intercalaciones pizarrosas de la capa de San Nicolás. Yacimiento de Almaden (Ciudad Real). *Estudios Geológicos* **1988**, *44*, 181–187.
62. Deng, C.; Lehmann, B.; Xiao, T.; Tan, Q.; Chen, D.; Tian, Z.; Wang, X.; Sun, G.; Yin, R. Intracontinental and arc-related hydrothermal systems display distinct δ202Hg and Δ199Hg features: Implication for large-scale mercury recycling and isotopic fractionation in different tectonic settings. *Earth and Planetary Science Letters* **2022**, *593*, 117646.
63. Wang, Q.; Morse, J.W. Pyrite formation under conditions approximating those in anoxic sediments I. Pathway and morphology. *Marine Chemistry* **1996**, *52*, 99–121.
64. Wang, X.; Shi, M.; Zhang, J.; Pang, Y.; Zhao, Y. Significance of trace elements in marine shale pyrite for reconstructing the sedimentary environment: a case study of Niutitang and Hongshuizhuang Formations. *ACS Earth and Space Chemistry* **2021**, *5*, 3210–3225.
65. Jones, D.S.; Fike, D.A. Dynamic sulfur and carbon cycling through the end-Ordovician extinction revealed by paired sulfate–pyrite δ34S. *Earth and Planetary Science Letters* **2013**, *363*, 144–155.
66. Audétat, A. The metal content of magmatic-hydrothermal fluids and its relationship to mineralization potential. *Economic Geology* **2019**, *114*, 1033–1056.